JOURNAL OF GEOPHYSICAL RESEARCH, VOL. 102, NO. D24, PAGES 29,625–29,640, DECEMBER 26, 1997

Seasonal AVHRR multichannel data sets and products for studies of surface-atmosphere interactions

J. Cihlar, J. Chen, and Z. Li
Canada Centre for Remote Sensing, Ottawa

Abstract. A basic methodological premise in the design of the Boreal Ecosystem-Atmosphere Study (BOREAS) is that the findings and models obtained at the stand level can be applied at the landscape, regional and global levels by using spatially comprehensive data sets, in particular satellite observations and meteorological measurements. Since many of the processes of interest are strongly influenced by solar radiation, satellite measurements at optical wavelengths are of fundamental importance. We describe a satellite data set and derived products prepared for the studies of the ecosystem-atmosphere interactions, including the scaling up of site and landscape measurements, model development and validation, and many other applications. It is derived from daily measurements by the advanced very high resolution radiometer (AVHRR) onboard the NOAA 11 satellite. The data set was obtained through a compositing process to minimize the contamination by clouds. Subsequently, the ABC3 procedure [*Cihlar et al.*, 1997] was applied to remove atmospheric attenuation effects, identify residual clouds or snow-covered pixels and remove the effect of this contamination, remove bidirectional reflectance effects, and correct for surface emissivity effects. The paper briefly reviews the correction procedures, discusses the characteristics of the corrected data set, and presents several derived products of biophysical parameters, including leaf area index and the fraction of photosynthetically active radiation, vegetation index accumulated over the growing season, and the daily total absorbed photosynthetically active radiation.

1. Introduction

Land biosphere, and vegetation in particular, is a crucial component of the global climate system. It is intimately linked with the global biogeochemical and hydrological cycles, and by determining the partitioning of incident solar radiation, it plays a critical role in the dynamics of the planetary boundary layer through which the surface-atmosphere interaction takes place. For these reasons a prime focus of the Boreal Ecosystem-Atmosphere Study (BOREAS) [*Sellers et al.*, 1995] was the understanding and characterization of the processes governing the interactions between the ecosystem and the atmosphere at diurnal and seasonal scales.

Although the interactive surface-atmosphere processes ultimately take place at the molecular and cellular level, they must be characterized at larger spatial scales. This is necessary because most of the variability and dynamics of interest occurs at landscape, region, and global levels. It is at these larger scales that the impact of seasonal and interannual variability is most directly experienced by other components of the natural or anthropogenic environment. In the "scaling up," i.e., extending the knowledge and understanding of detailed process studies from small sites to the area beyond, satellite remote sensing provides the principal tool. Thus the second overarching objective of BOREAS was to "develop and validate remote sensing algorithms to transfer our understanding of the above processes from local scales out to regional scales" [*BOREAS Science Steering Committee*, 1991].

Since much of the biosphere-atmosphere interaction is determined or conditioned by solar radiation, remote measurements at optical and thermal infrared wavelengths are the remote sensing technique of choice. Unfortunately, surface observations at optical wavelengths are complicated by the ubiquitous presence of clouds, haze, and other sources of noise. This limitation can be substantially mitigated by frequent observations. For example, wide-angle optical satellite sensors provide daily coverage of the entire globe, thus increasing the likelihood of obtaining a clear-sky view of the surface. These sensors have thus become an important source of information about the characteristics and dynamics of the land biosphere at regional and global scales. Their unique strengths, afforded by daily coverage and the sensitivity to ecosystem processes, have been demonstrated with data from the advanced very high resolution radiometer (AVHRR) onboard NOAA satellites for over a decade [e.g., *Gatlin et al.*, 1984]. These successes have led to the construction of several similar sensors to be launched in the late 1990s and early 2000: VEGETATION onboard SPOT 4 in 1997 [*Saint*, 1994], MODIS on the first NASA Earth Observing System platform AM 1 [*Salomonson*, 1988], and MERIS on the ESA Envisat.

At regional scales, clouds are always present in the images. Compositing procedures [*Holben*, 1986] are therefore used to create nominally cloud-free data sets over periods of several days when the surface conditions may be considered static. High-performance computer systems have been designed to process large volumes of data in this manner [*Roberston et al.*, 1992; *Eidenshink and Faundeen*, 1994]. Although the resulting composite images are mostly cloud free, they nevertheless contain some cloud-contaminated pixels, either fully (which are easily detectable) or in part. Other sources of noise are angular

Published in 1997 by the American Geophysical Union.

Paper number 97JD01195.

variations in reflectance as a function of the Sun-target-sensor geometry which fluctuates with surface cover type and season, atmospheric effects (absorption and scattering by gases and aerosols), and surface emissivity in the thermal infrared channels. These noise sources obscure the signal from the vegetated surfaces and interfere with the extraction of quantitative information from the optical satellite data. The removal of such noise must therefore precede the estimation of biophysical parameters from the optical data.

The objective of this paper is to describe a data set based on AVHRR data which was developed for regional scaling in BOREAS, to assess its characteristics, and to discuss several derived products representing biophysical parameters of the surface environment.

2. Data and Methodology

Data from the advanced very high resolution radiometer (AVHRR) onboard NOAA 11 satellite [*Kidwell*, 1991] were used as the basic data source. The choice was determined primarily by continuity with related programs, e.g., the Pathfinder data set [*James and Kalluri*, 1994] and the proximity of the local time of overpass to early solar afternoon. The period was chosen so as to include the growing season, starting on April 11, 1994, but ending prematurely after September 10 due to the failure of the sensor. All five AVHRR channels were processed. Data processing was carried out in two main phases, one resulting in "raw" composite images and the other in "refined" data sets. The first phase (sections 2.1 through 2.3 below) was carried out using the high-throughput geocoding and compositing system (GEOCOMP) [*Robertson et al.*, 1992], developed jointly by Canada Centre for Remote Sensing (CCRS) and MacDonald Detwilers and Associates and operated by the Manitoba Remote Sensing Centre; the second phase (sections 2.4 through 2.9) was completed in house using a methodology dubbed ABC3 (atmospheric, bidirectional, and contamination corrections of CCRS) [*Cihlar et al.*, 1997].

2.1. Calibration

All five AVHRR channels were calibrated. Since NOAA satellites do not support onboard calibration for the optical channels 1 and 2, the calibration was done in two steps: first converting raw digital signal level into at-sensor radiance and, secondly, representing the resulting radiance on a fixed 10 bit output scale as calibrated digital signal level [*Teillet and Holben*, 1994]. For the 1994 data, NOAA 11 GEOCOMP used time-dependent (defined as days since launch) correction of the AVHRR gain and offset of the channels 1 and 2 [*Cihlar and Teillet*, 1995]. The thermal AVHRR channels 3–5 were calibrated using onboard calibration data as specified by NOAA [*Planet*, 1988]. It should be noted that the correction method does not deal with the effects of sunlight impinging on an internal blackbody target of the satellite or the inclusion of a quadratic calibration effect for these thermal channels. The resulting values are in radiance units ($W/m^2/sr/mm$ for channels 1 and 2 and $MW/m^2/sr/cm^1$ for channels 3–5).

2.2. Geometric Registration

The correction of each input image for geometric distortions is necessary to ensure that pixels representing the same surface area are compared in the compositing process. The following distortions were taken into account by GEOCOMP: spacecraft orbit and attitude, spacecraft velocity and altitude, Earth rotation, and Earth curvature. Correction parameters for the above errors were derived from a combination of the input images, auxiliary data, and known satellite/sensor parameters. A systematic orbit model was generated from the orbital elements supplied in the data stream and is then refined by using autocorrelation between the pass of input imagery and high-resolution image chips associated with ground control points. Operator selection of ground control points is the backup mode. The image chips were created from Landsat MSS or MOS MESSR images (spatial resolution of about 50 m). GEOCOMP typically achieves a measured two-dimensional root-mean-square absolute error around 600 m for its single-date, 1 km pixel size scenes for control points used to refine the orbit model. The overall registration accuracy of an image depends, to a considerable degree, on the spatial distribution of the control points in the image. Given that clouds typically cover large contiguous parts of AVHRR images, the misregistration can exceed 1 km in parts of the single-date image. In addition, because of the compositing process where images are combined whose registration errors can add up the relative registration accuracy within the composite can be substantially lower than that of a single scene. The variable resolution of the data caused by different view zenith angles also reduces geometric accuracy [*Cihlar et al.*, 1996]. When the transformation to the map projection was established, the input image was resampled from the satellite projection to Lambert conformal conic projection (reference latitudes 49°N and 77°N, reference meridian 100°W) using Kaiser window damped 16 point $(\sin x)/x$. The same resampling was applied to all AVHRR channels.

2.3. Compositing

Individual images obtained over 10 day periods (the last period of each month starts on the 21st) were combined through a compositing process. The maximum value of the normalized difference vegetation index (NDVI) computed from top-of-the atmosphere (TOA) radiances was used to select the most cloud-free pixel available for the period. Although other compositing algorithm options with better performance have been considered [*Cihlar et al.*, 1994], maximum NDVI is still the most often used compositing criterion [e.g., *Eidenshink and Faundeen*, 1994; *James and Kalluri*, 1994] and has known biases. Only pixels with view zenith angles below 57° were eligible for compositing; this threshold was selected as a compromise between obtaining good temporal resolution and avoiding large off-nadir angles. When the pixel/date were selected, a composite image was created which includes AVHRR channels 1–5, solar zenith (q_s) and view zenith (q_v) angles, the relative azimuth angle (difference between the solar and the sensor azimuth angles, f), and the date when the selected pixel was recorded. All channels were recorded in 16 bits so as not to degrade the original 10 bit quantization. The above processing thus yielded 10 channels of data for 15 periods in 1994.

2.4. Computation of Top-of-Atmosphere Reflectance

TOA reflectance for channels 1 and 2 was calculated from the corrected radiance (see *Teillet* [1992] and *Cihlar et al.* [1996] for details).

2.5. Atmospheric Correction of AVHRR Channels 1 and 2

The simplified method for atmospheric correction algorithm (SMAC) [*Rahman and Dedieu*, 1994] was employed in the processing. The pixel-based angular information is provided in

the basic data set. The program also requires vertically integrated gaseous contents and the value of aerosol optical depth at 550 nm for each pixel. The processing was carried out assuming water vapor content of 2.3 g/cm^2 and ozone content of 0.319 cm atm. In the absence of actual data for optical depth at 550 nm, a constant value of 0.05 was used. This value had also been recommended by *Teillet* [1992] for clear-sky conditions, based on extensive atmospheric transmission measurements during the growing season in eastern Canada [*Ahern et al.*, 1991]. It should be noted that the accuracy of 5S decreases if q_s and q_v are above 60° and 50°, respectively, or if the optical depth is above 0.8 [*Rahman and Dedieu*, 1994]. Since the solar zenith angle (SZA) ranged between about 55° and 70° during the 1994 season due to the late local time of overpass, the SMAC algorithm itself likely contributed noise to the atmospheric corrections, in addition to the errors caused by the differences between the actual and the assumed state of the atmosphere. SMAC was applied sequentially to all 15 composites. The processing resulted in surface reflectance for AVHRR channels 1, 2, and NDVI which were then used in subsequent calculations.

2.6. Identification of Contaminated Pixels

A new procedure dubbed CECANT (cloud elimination from composites using albedo and NDVI trend) was developed to identify pixels contaminated by local atmospheric effects or snow [*Cihlar*, 1996]. CECANT is based on high NDVI sensitivity to the presence of clouds, aerosols, or snow. Three features of the seasonal surface reflectance trend are used: (1) the high contrast between the albedo (represented by AVHRR channel 1) of land, especially when fully covered by green vegetation as opposed to clouds or snow/ice; (2) the expected NDVI value for that pixel and compositing period; and (3) the monotonic NDVI trend (increase to peak green, decrease thereafter). For a given pixel (i, j) and compositing period t, two intermediate variables are calculated, $R_{i,j,t}$ and $Z_{i,j,t}$. R measures the deviation of $\mathrm{NDVI}_{i,j,t}$ from the expected average value in units of "average scatter" (represented by median) around the seasonal curve. Z measures the magnitude of NDVI decrease between dates and assumes that large and rapid NDVI decreases are not caused by surface changes. Four threshold values are required to identify a partially contaminated pixel; these were derived by using the means of R_t and Z_t histograms for all Canada. Prior to the application of CECANT $\mathrm{NDVI}_{i,j,t}$ values were corrected for solar zenith angle effects, following the procedure of *Sellers et al.* [1994] and using the land cover map of *Pokrant* [1991]. The new set of NDVI values was then computed for a reference $q_s = 45°$ based on the equations of *Sellers et al.* [1994]. Details on this correction are given by *Cihlar et al.* [1997].

2.7. Corrections for Bidirectional Reflectance Effects in Channels 1 and 2

Bidirectional dependence is prominent in many land cover types observed over the BOREAS region [*Li et al.*, 1996]. Reflectances at extreme viewing angles are 2–4 times larger than those observed near nadir. Correction for such effects is thus critical to many remote sensing applications. The model of *Roujean et al.* [1992] as modified by *Wu et al.* [1995] was used to characterize the seasonal bidirectional reflectance distribution function (BRDF) for each cover type. Only clear-sky pixels were included in the derivation of the model coefficients, and no bidirectional corrections for snow- or ice-covered areas were made. The BRDF is given by

$$\Omega_i(\theta_s, \theta_v, \phi) = \frac{\rho_{s,i}(\theta_s, \theta_v, \phi)}{K_0} = 1 + a_1 \cdot f_1(\theta_s, \theta_v, \phi) + a_2 f_2(\theta_s, \theta_v, \phi), \quad (1)$$

where $r_{s,i}$ denotes the surface reflectance in channel i; a_1 and a_2 are the weighting factors of the two kernels given by f_1 and f_2. Their values were obtained for each cover type using a sample of pixels selected from the data set, following the method described by *Li et al.* [1996]. The present approach is different from that of *Wu et al.* [1995] and *Li et al.* [1996] in that the bidirectional correction is done after the atmospheric correction. We employed AVHRR-derived land cover map of Canada with pixel size of 1 km (Plate 1) to determine cover type, omitting the outer pixel in all land cover polygons to minimize the impact of misregistration errors. With (1), a measurement made for a specific illumination and viewing geometry can be normalized to a common Sun-target-sensor geometry. From an observed reflectance $r_{s,i}(q_s, q_v, f)$ the normalized reflectance at $q_s = 45°$, $q_v = 0°$, and f of any value is determined by

$$\rho_{s,i}(45°, 0°, \phi) = \frac{\Omega_i(45°, 0°, f)}{\Omega_i(\theta_s, \theta_v, \phi)} \rho_{s,i}(\theta_s, \theta_v, \phi). \quad (2)$$

Following this procedure, a pair of channels 1 and 2 images with a constant viewing geometry ($q_v = 0°$, $q_s = 45°$) were obtained for each of the 1994 compositing periods. In addition, the BRDF model can be used to derive an albedo defined in the upper hemisphere $A_{s,i}(q_s)$, from a reflectance observed from a specific direction $r_{s,i}(q_s, q_v, f)$:

$$A_{s,i}(\theta_s) = \frac{\rho_{s,i}(\theta_s, \theta_v, \phi)}{\pi \Omega_j(\theta_s, \theta_v, \phi)} \int_0^{2\pi} \int_0^{\pi/2} \Omega_j(\theta_s, \Theta_v, \Phi) \cdot \cos \Theta_v \sin \Theta_v \, d\Theta_v \, d\Phi \quad (3)$$

2.8. Replacement of Contaminated Pixels for AVHRR Channels 1 and 2

Two cases were recognized, pixels contaminated (1) during or (2) at the end of either end of the observed period. For pixels during the growing season, it was assumed that no rapid changes would occur between adjacent 10 day periods, and the missing values could therefore be linearly interpolated using the seasonal trajectory for that pixel/channel. To allow replacement of values contaminated on September 1–10, composite images from 1993 were used after 10 September 10, 1994, and linear interpolation was applied. For pixels contaminated on April 11–20, 1993, data after September 11 and an interpolation procedure detailed by *Cihlar et al.* [1997] was employed. Thus the pixels replaced near the ends of the 1994 measurement series may not be accurate, especially for September 1–10 in pixels where significant change in land cover occurred during 1994 (e.g., forest fire).

2.9. Smoothing NDVI Trajectories

The NDVI data were smoothed, using the temporal dimension of the data set. The smoothing algorithm was simple: for each compositing period t, examine five values ($t - 2$ through $t + 2$), delete the lowest and the highest value, and average the remaining three values to obtain $\mathrm{NDVI}_{i,j,t}$.

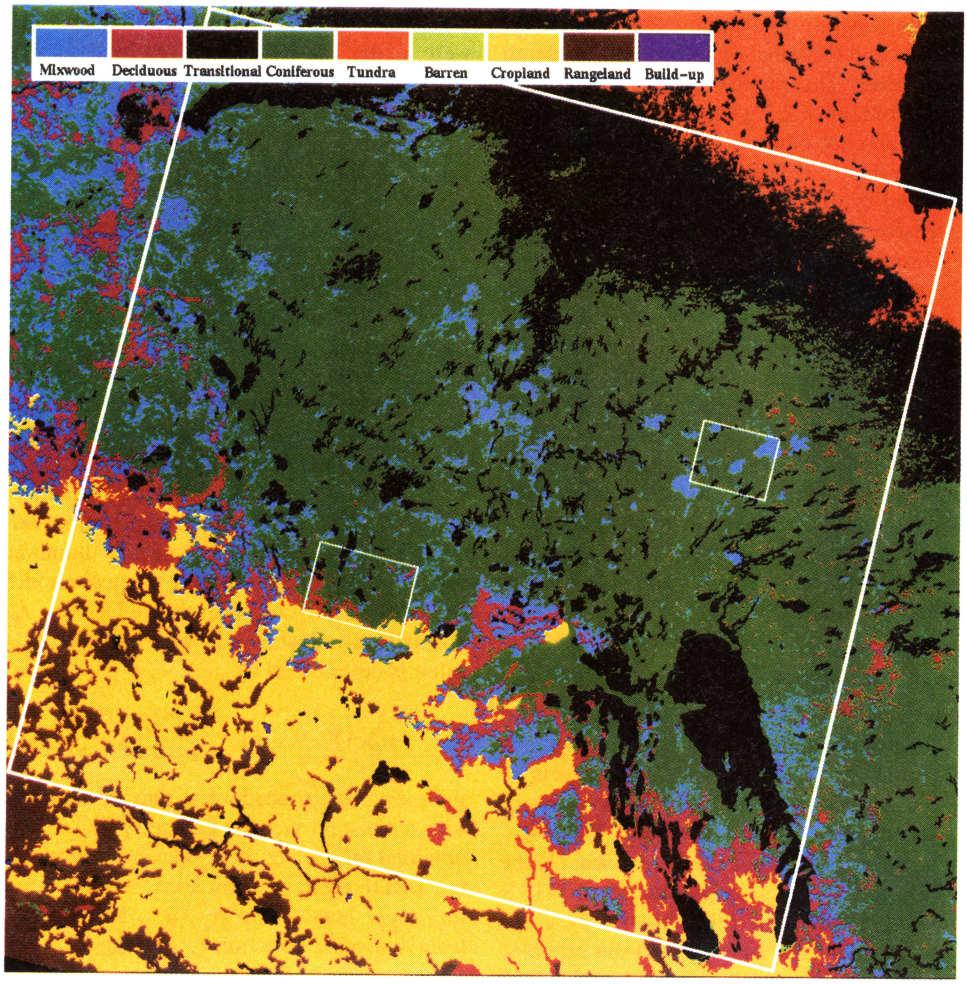

Plate 1. A generealized land cover map of the study area [from *Pokrant*, 1991].

2.10. Channel 4 Correction

The goal of the processing of the thermal channel was to obtain pixel-based surface temperature information for each period t, based on the composite channels 4 and 5 data from section 2.3 above. The modified split window method of *Coll et al.* [1994] was used which accounts for both atmospheric and surface emissivity effects. Coefficients estimating atmospheric effects at midlatitudes were derived by *Coll et al.* [1994]. For soil and vegetation emissivities in channels 4 and 5, a combination of sources was used [*Salisbury and D'Aria*, 1992; *Becker and Li*, 1990]. The nonlinear relationship between the surface emissivity and the NDVI [*Van de Griend and Owe*, 1993] was used to estimate emissivity for channel 4 as well as the difference in emissivities between channels 4 and 5. After computing the surface temperature, only pixels contaminated during the growing season were replaced similarly as for channels 1 and 2; this was done to preserve the information on the length of the growing season. Additional information on the processing methodology is provided by *Cihlar et al.* [1997].

3. Results and Discussion

3.1. Effectiveness of ABC3 Corrections

Figure 1 shows an example of the effect of the various corrections on AVHRR channels 1 and 2 data for coniferous forest pixels in midsummer. TOA values for all pixels cover a wide range. The backscatter reflectances (shown with negative view zenith angle) are higher than corresponding forescatter values, consistently with results reported elsewhere [*Wu et al.*, 1995; *Li et al.*, 1996; *Cihlar et al.*, 1994]. Reflectance decreases after atmospheric corrections, especially in channel 1 because of the removal of the Rayleigh scattering effect (second panel of Figure 1). The range of reflectances decrease significantly once the cloud-contaminated pixels are removed (third panel of Figure 1). Finally, the bidirectional reflectance corrections removed most of the angular dependence of reflectance (bottom panel); the residual scatter represents mostly the variable reflectance of the forest and the admixture of other cover types, both as mixed pixels and due to inaccurate land cover type information. Results reported elsewhere [*Li et al.*, 1996; *Cihlar et al.*, 1997] show that the bidirectional reflectance correction procedure removes about 50–70% of the viewing geometry-dependent variability, depending on the data set and AVHRR channel.

In addition to the validation results reported by *Cihlar et al.* [1997] a partial validation of the ABC3 procedure was carried out as part of the development of biophysical parameter products based on NDVI. Landsat Thematic Mapper (TM) images (61 km × 61 km area) were first corrected for atmospheric effects using 5S (*Tanre et al.* [1990], midlatitude summer atmosphere and visibility of 30 km at sea level). TM images were then coregistered with the GEOCOMP images in the corre-

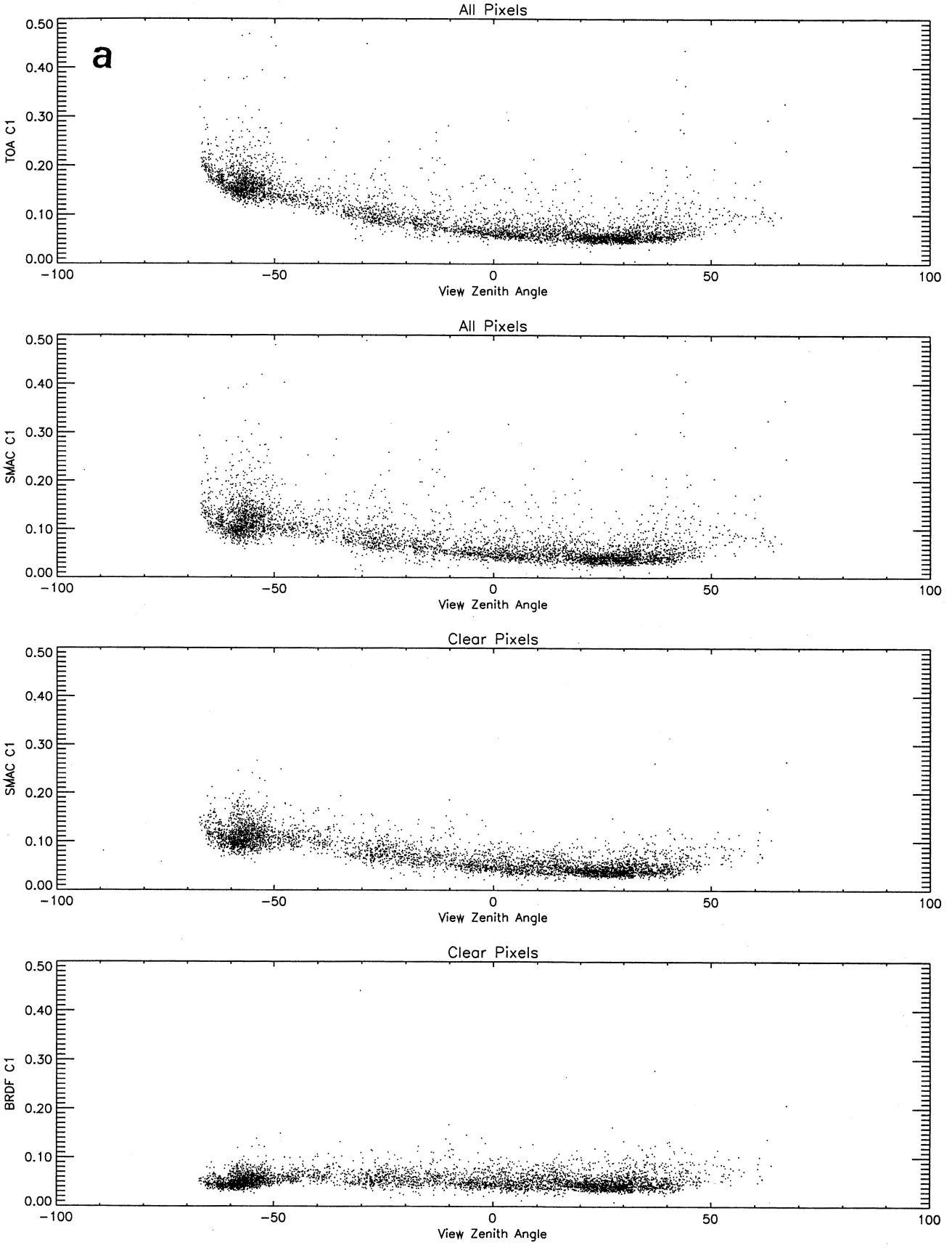

Figure 1. Effect of the data corrections on the advanced very high resolution radiometer (AVHRR) channel 1 (Figure 1a) and channel 2 (Figure 1b) data over the BOREAS region, July 11–20, 1993. The four panels show the following: scattergrams of the land pixels for top-of-atmosphere (TOA) reflectances (all pixels), reflectances after atmospheric corrections (all pixels), reflectances after eliminating contaminated pixels (clear-sky pixels), and reflectances after bidirectional reflectance corrections. Only coniferous forest pixels are shown.

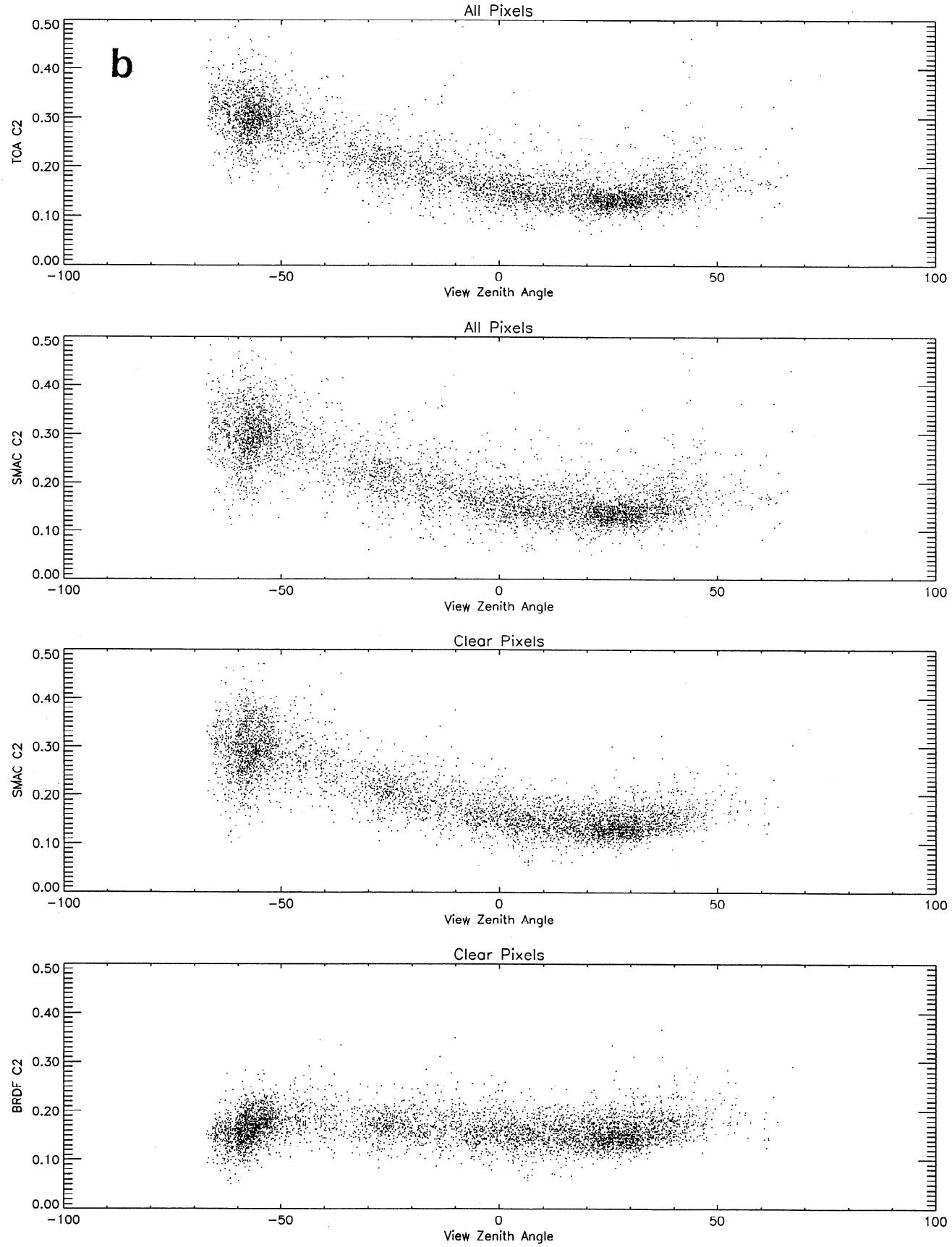

Figure 1. (continued).

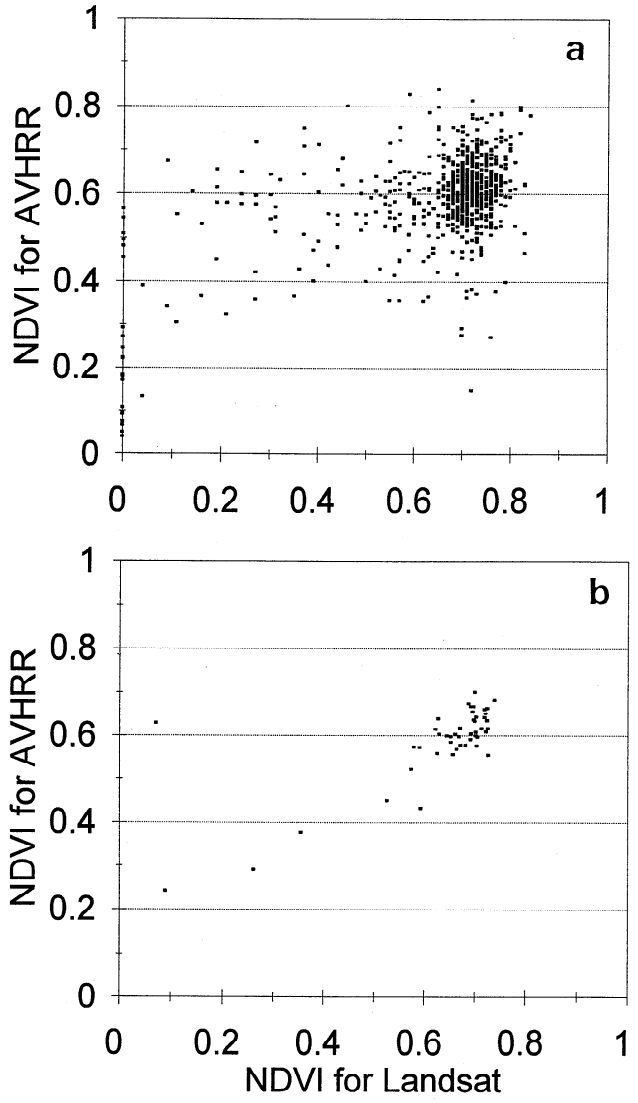

Figure 2. Comparison of normalized diffence vegetation index (NDVI) from 1994 corrected AVHRR data (computed from C1 and C2 corrected for atmospheric and bidirectional reflectance distribution function (BRDF) effects) and Landsat Thematic Mapper (TM) data, for 1 × 1 km pixels (Figure 2a) and 4 × 4 km pixels (Figure 2b). Landsat TM pixels were averaged to the pixel sizes indicated.

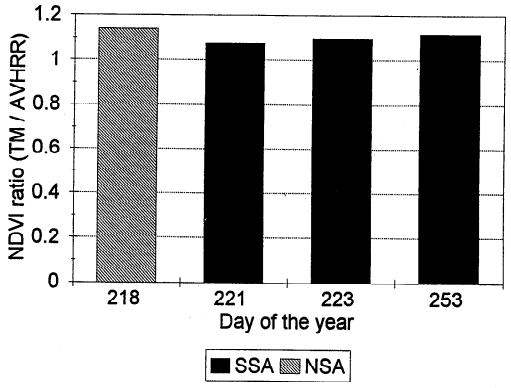

Figure 3. Comparison of NDVI from 1994 corrected AVHRR data (computed from C1, C2 corrected for BRDF effects) and Landsat Thematic Mapper data for site average (61 × 61 km). Landsat TM pixels originate from various years: day 218, August 6, 1992; day 221, August 9, 1991; day 223, August 11, 1986; day 253, September 10, 1991.

sponding time periods using common surface features (lake edges and centers, islands, etc.) as the ground control points. The accuracy of the coregistration was found to be ±1 pixel (1 km), limited by the difficulty in locating corresponding control point pairs. After the registration the TM pixels were averaged to 1 km resolution. Figure 2a shows NDVI from AVHRR against NDVI from TM. The scatter of the data points is considerable due to (1) misregistration because the variation in NDVI from one pixel to the next can be high; (2) resampling because an AVHRR pixel after resampling from an originally larger pixel is affected by neighboring pixels [*Cihlar et al.*, 1996], while a TM pixel resampled to 1 km represents the true mean NDVI value of that pixel; (3) incomplete atmospheric corrections due to imperfect knowledge of the atmospheric state; (4) differences in the solar zenith angles and differences in the year of data acquisition. The scatter indicates the complexity in obtaining accurate NDVI values at the 1 km scale using AVHRR measurements.

In order to derive a single radiometric correction factor for the AVHRR-derived NDVI, a 4 × 4 pixel window averaging was performed on both TM and AVHRR images (Figure 2b). Most of the scatter was reduced, suggesting that the inaccuracy in registration and the artifacts introduced through resampling and compositing are the main causes of the large scatter in Figure 2a. It should be noted that the AVHRR intercept at the ordinate (as TM NDVI decreases to zero) does not necessarily reduce to zero. This is due to the effect of larger AVHRR pixels at higher view zenith angles. Where adjacent pixels with high and low NDVI occur (e.g., near the edge of open water), the large AVHRR pixels have NDVI in which the higher-NDVI component surface tends to dominate (e.g., land with much higher NDVI than open water). After resampling, this dominant effect of the "brighter" cover type is spread over a larger area. One consequence is a decrease in the apparent size of water bodies in the composite images. Since the TM data are averaged strictly within the specified pixel size (4 km in this case), the NDVI difference is most evident at the low NDVI values, thus resulting in the nonzero intercept. The intercept causes a difficulty in determining a single correction factor because the slope cannot be used in this case. To find the correction factor, the NDVI values were compared only for land pixels (where the NDVI contrast is smaller), i.e., the top part of the data range in Figure 2. This is done by first computing linear regression between these two series of data and then calculating the AVHRR NDVI at the TM NDVI value representing the center of the higher cluster of the data points.

Figure 3 shows the correction factor as a ratio of the NDVI values between TM and AVHRR determined for four TM images. The mean of the value is 1.10, suggesting that on average, Landsat TM NDVI is 10% larger than the AVHRR NDVI over land surface areas. The major reason for the larger TM NDVI values lies in the broader AVHRR visible band (571–684 nm) than in the TM red band (622–699 nm). The AVHRR visible band contains green wavelengths which have larger reflectance values than red wavelengths over terrestrial surfaces. Other factors, including difference in view geometry and solar zenith angle, may also have small effects on the

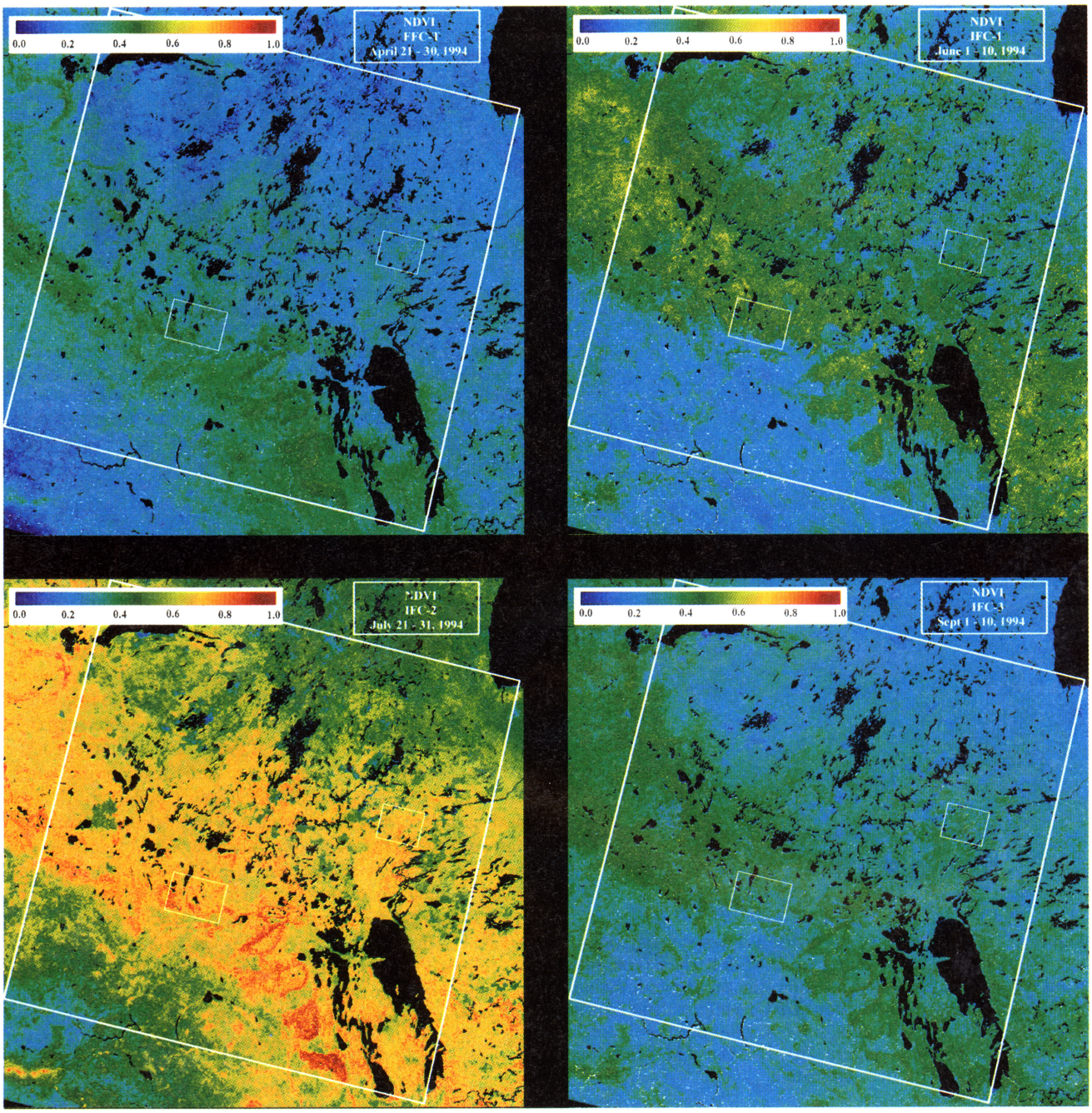

Plate 2. Normalized difference vegetation index (NDVI) for the BOREAS Region during four 1994 field campaigns: (top left) FFC-T, April 21–30; (top right) IFC-1, June 1–10; (bottom left) IFC-2, July 21–31; and (bottom right) IFC-3, September 1–10. The three squares outline the BOREAS region and the northern and southern study areas, respectively.

difference. This 10% correction to NDVI is important because the derivation of surface parameters is very sensitive to changes in NDVI. For example, *Chen and Cihlar* [1996] found that a difference of 5% in NDVI can cause leaf area index (LAI) to change by 20%.

3.2. Vegetation Index and Surface Temperature Trends

Plate 2 illustrates the seasonal progression of NDVI during the BOREAS field campaigns. The dramatic change between April and July is primarily due to the deciduous forest and (after June) the agricultural area south of the boreal forest, although the coniferous forest also showed some increase in NDVI. By early September the deciduous forest dominated NDVI distribution. The seasonal changes in the NDVI pattern strongly suggest that understory plays an important role (e.g., compare June and September images); however, the precise effects of overstory and understory are not well understood at present. These effects could be unraveled more effectively if the overstory and understory have different temporal trajectories, or if allometric relations could be established between the two (possibly as a function of site conditions). This area requires more work.

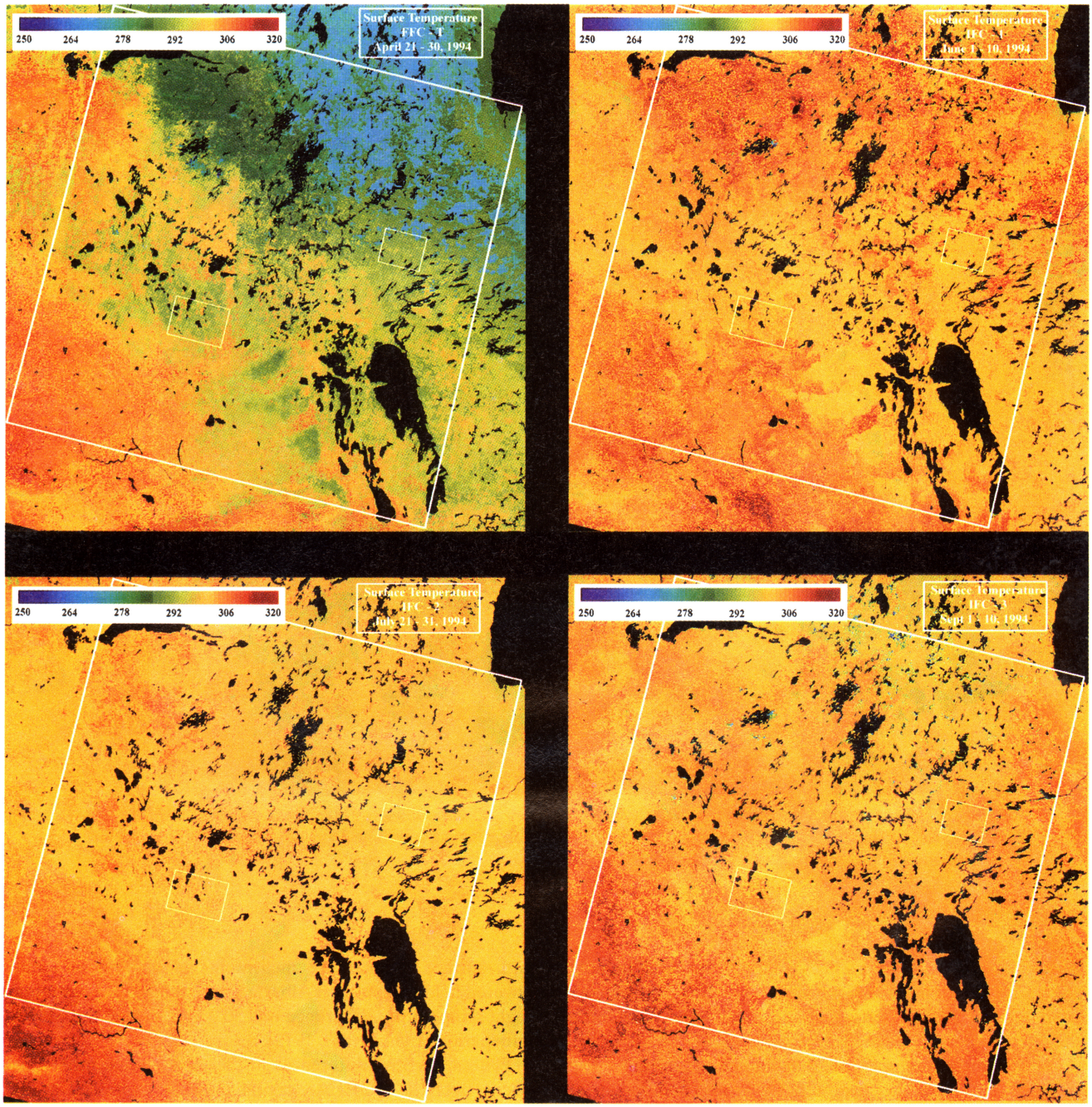

Plate 3. Surface temperature obtained from composite AVHRR data during four 1994 field campaigns: (top left) FFC-T, April 21–30; (top right) IFC-1, June 1–10; (bottom left) IFC-2 July 21–31; and (bottom right) IFC-3 September 1–10. The three squares outline the BOREAS region and the northern and southern study areas, respectively.

Composite images of surface temperatures for the same periods are shown in Plate 3. The seasonally persistent features are Porcupine Hills and Pasquia Hills west of Lake Winnipegosis and the warmer SW grassland region with lower NDVI. The visibility of the hills is mainly due to the contrast with the surrounding landscape and is most likely due to a combination of topographic and vegetation effects (Plate 1). In April the northern area was cold due to the previous snow cover, but in the summer, the tundra at the northern edge of the boreal forest and cropland adjacent to the south had similar surface temperatures. It is worth noting that in the early June the area north of the boreal forest was as warm as the grassland in the southwest. This indicates high sensible heat loss and explains the thick boundary layer which was observed during the second intensive field campaign [*Sellers et al.*, 1995]. Also, in the early summer the forest burns (shown as red patches in Plate 3, top right) had markedly higher temperatures than surrounding areas. This difference diminished during the summer as the herbaceous vegetation developed (compare Plate 3, top right and bottom left, with Plate 2, top left and bottom right). The sharp edge in Plate 3, top right, is a remaining artifact caused by the differences in imaging dates in the composite data set. It is interesting to note that in July and September the afternoon temperatures were similar over the entire area, in spite of

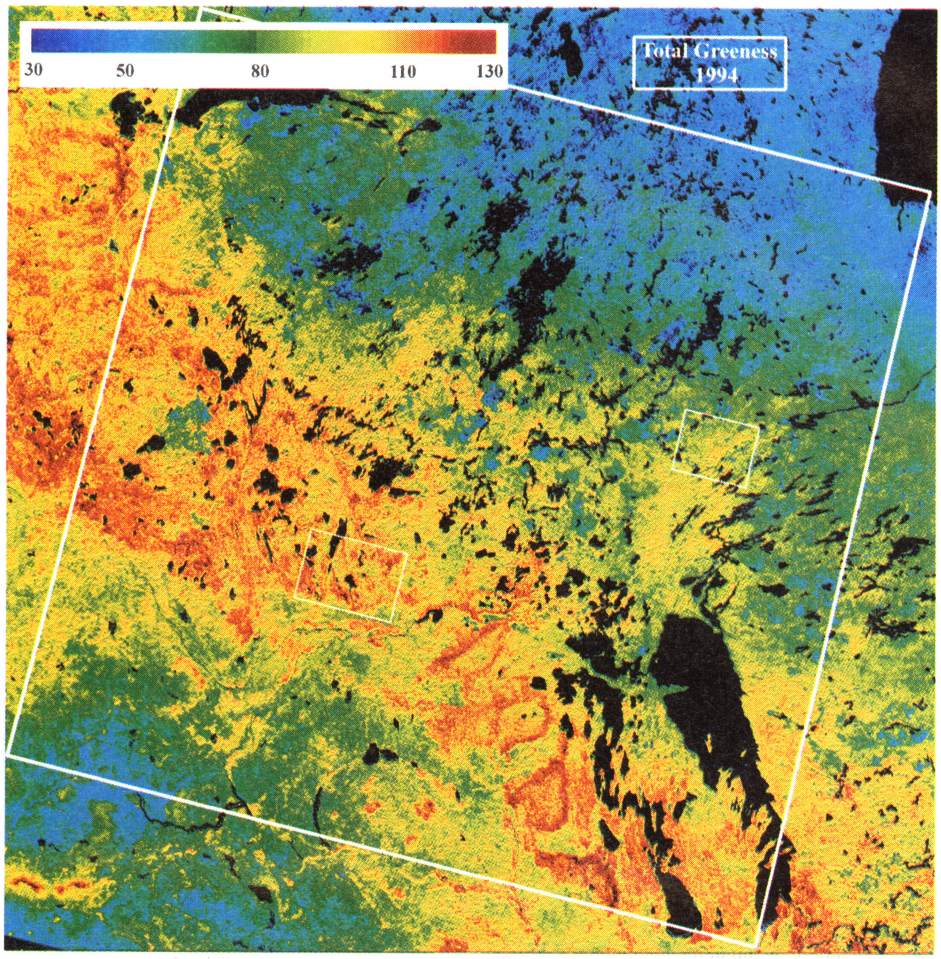

Plate 4. Area under the NDVI curve during the 1994 growing season. The three squares outline the BOREAS region and the northern and southern study areas, respectively. The 1993 data were used for the last part of the 1994 growing season (see text for explanation).

the substantial NDVI differences (Plate 2). It should be noted that local variations in the surface temperature values could exist due to the differences in the local solar time during satellite overpass.

Overall, surface temperatures in the area seem quite high. We have examined the possibility that these high values are caused by the processing, especially the atmospheric and emissivity corrections. As *Cihlar et al.* [1997] showed, the split window correction is comparable to those produced by other atmospheric correction methods for thermal infrared data, while the emissivity correction (constrained by extreme values of 0.955 and 0.985) was <2°C in most cases, decreasing with an increasing emissivity. We have compared the AVHRR surface temperatures with daily maximum air temperature values in 1993 (AVHRR data processed the same way) and found an average offset of +5°C (not shown). *Wooster et al.* [1995] found that the prelaunch central wavenumber for channel 5 of the NOAA 11 AVHRR was not correctly specified, leading to an error in channel 5 temperatures of about 0.4°C. This could introduce a potential error of about 0.6°C. The +5°C variation could be explained by the difference between surface and air temperatures, supplemented by the error in channel 5 temperature (see also *Czajkowski et al.* [1997]) and imprecise emissivity corrections. The high surface temperatures are consistent with surface temperature measurements of bare or straw-covered fields in southern Alberta where the surface day minus night temperature difference was 30°–35°C during the May to July period [*Cihlar et al.*, 1979].

Plate 4 portrays differences in the total photosynthetic capacity over the BOREAS region in 1994, expressed as the accumulated NDVI over the growing season. It was produced by identifying the starting and ending date for the growing season, defined as the first and last date when surface temperature exceeded +10°C; this value was chosen instead of the usual +5°C to compensate for the fact that the latter represents the average daily temperature. The composite date was considered to be the middle of the 10 day period and the exact starting/ending date was obtained through linear interpolation. When the growing season period was identified for each pixel, the NDVI values were accumulated, also using linear interpolation for individual days. Plate 3 shows that the maximum photosynthetic capacity was associated with the forested region, especially deciduous. Even the transitional forest showed higher values than cropland in spite of the shorter length of the growing season, evidently because of the higher NDVI values over a shorter period. This contrast is also well shown in the Cypress Hills (bottom left-hand corner of Plate 4) in which coniferous forest is surrounded by cropland and grassland.

3.3. Leaf Area Index (LAI)

LAI is defined as half of the total leaf area per unit ground surface area [*Chen and Black*, 1992]. This definition is an improvement over previous definitions based on projected or one-sided leaf area when used for leaves of different shapes. Three LAI maps shown in Plate 5 were produced using corrected NDVI images for the periods of June 1–10, July 21–31, and September 1–10, 1994 (corresponding to BOREAS intensive field campaigns IFC-1, IFC-2, and IFC-3). Similar LAI maps were generated for other 10 day AVHRR composite images during the growing season of 1993 and 1994. The maps show the seasonal and spatial variations in LAI. In general, LAI increases from IFC-1 to IFC-2 in the spring and then decreases from IFC-2 to IFC-3 in the fall. The changes are most pronounced in the prairie agricultural areas and in the deciduous forests near the southern edge of the boreal forest. Changes in the tundra north of the boreal forest are also noticeable.

In the calculation of LAI from NDVI, a land cover map [*Pokrant*, 1991] was used and different algorithms were employed for the following 10 land cover types: water; mixed-wood, deciduous, coniferous, and transitional forest; tundra; barren lands; cropland; rangeland/pasture; and built-up areas. For water, barren lands, and built-up areas, LAI was assigned zero. An algorithm for cropland was formulated using published NDVI-LAI relationships [*Holben et al.*, 1980; *Gardner and Blad*, 1986; *Aase et al.*, 1986; *Wiegand et al.*, 1992; *Li et al.*, 1993]. The algorithm for coniferous forests was derived from our recent work [*Chen and Cihlar*, 1996]. The deciduous forest algorithm is based on *Chen et al.* [1997]; it is less accurate than that for conifers because of the seasonal vegetation dynamics and insufficient field data for temporal coverage. Mixed wood and transitional forests were considered as intermediate cases between coniferous and deciduous forests. Tundra and rangeland/pasture were treated the same as cropland because of the lack of cover type-specific field data.

In the LAI calculation, different algorithms were used for the different periods in an attempt to remove the understory contribution to the measured NDVI signal. However, this approach presently has varying degrees of success across the landscape. In jack pine stands with lichen as the background, the understory contribution is generally small. In black spruce, the green moss (*Sphagnum* sp. and *Pleurozium schreben*) cover and the predominant Labrador tea (*Ledum groenlandicum*) understory are difficult to differentiate from the overstory in the NDVI signal. Aspen stands generally have abundant hazelnut (*Corlus cornuta*) in the understory which has similar spectral signatures to the overstory and is even more difficult to differentiate. Therefore in the present product, the understory is included in the total LAI, and only the knowledge of the seasonal phenology for the overstory and understory can be used to qualitatively assess the presence of the two effects in the forested areas. We also conducted investigations on the possible improvement to be made using other surface-adjusted vegetation indices, but we found that NDVI and SR are the best among all because much noise is reduced when the ratio of the two bands is taken. Other indices involving more complicated munipulations of the signals tend to either retain or even amplify the noise in the measurements [*Chen*, 1996c].

Open boreal forests, especially black spruce (*Picea mariana*) and jack pine (*Pinus banksiana*), have a distinct canopy architecture which presents a challenge for measuring leaf area index. To quantitatively assess the effect of canopy architecture on optical LAI measurements, we recently developed a sunfleck-LAI optical instrument named the TRAC (tracing radiation and architecture of canopies). The TRAC measures the direct light transmitted through the canopy at short intervals (10 mm) and over long transects (up to 300 m) near the forest floor. Using the solar beam as a probe, a canopy gap size distribution can be calculated and a clumping index derived as a correction to LAI measurements based on gap fraction using instruments such as the LI-COR LAI-2000 [*Chen*, 1996a]. The TRAC has also been used to investigate the effect of blue light scattering on the LAI measurements with LAI-2000 [*Chen et al.*, this issue]. The TRAC technique has been validated and used for boreal forests [*Chen and Cihlar*, 1995a, b; *Chen et al.*, this issue]. The LAI algorithms for boreal forests were developed by first correlating ground-based LAI measurements with NDVI from Landsat TM, and using the algorithms at the AVHRR scale after the correction for the sensor difference with the ratio derived in Figure 3. At the present stage, no further corrections for the difference in spatial scales between TM and AVHRR are made. Our preliminary evaluation suggests that the scaling effect due to nonlinearity in the NDVI-LAI relationship and due to the discontinuity of NDVI at LAI = 0 between land surface and water is generally within 5% for pure land surfaces but considerably larger for mixed water and land pixels.

3.4. Fraction of Photosynthetically Active Radiation (FPAR)

FPAR is defined as the fraction of photosynthetically active radiation absorbed by a plant canopy. It excludes the fraction of incident PAR reflected from the canopy and the fraction absorbed by the soil surface, but it includes the portion of PAR which is reflected by the soil and absorbed by the canopy on the way back to space [*Chen*, 1996b]. Green FPAR refers to the fraction absorbed by green leaves only, after the removal of the contribution of the supporting woody material to the PAR absorption. The instantaneous green FPAR is integrated over the day length with a weight equal to the cosine of the solar zenith angle to obtain the daily green FPAR presented in the map. With this weighting scheme the daily green FPAR can be used as a parameter to convert the daily absorbed PAR to daily total incident PAR.

The green FPAR map shown in Plate 6 is produced for the period of July 21–31, 1994, corresponding to the BOREAS IFC-2. Similar maps were produced for other 10 day composite dates during the growing seasons of 1993 and 1994. Boreal conifer forests have the moderate FPAR values with a mean value close to 0.6. Deciduous forests at the southern border of boreal forests show larger values, partly due to the effect of the understory. Agricultural areas have also large FPAR values (range 0.8–0.9) in the summer, but the values for grassland and tundra are much lower.

Similar to the calculation of LAI, different algorithms for the daily green FPAR were used for the 10 land cover types. FPAR for water, barren lands, and built-up areas is assumed to be zero. An algorithm for the cropland was formulated using data by *Asrar et al.* [1984]. The algorithms for the coniferous forest are given by *Chen* [1996b]. The algorithm for deciduous forest is similar, but its coefficients were adjusted to match FPAR measured with TRAC. Tundra and rangeland/pasture were treated the same as cropland because of lack of data.

In Plate 6 the values for boreal forests are most reliable.

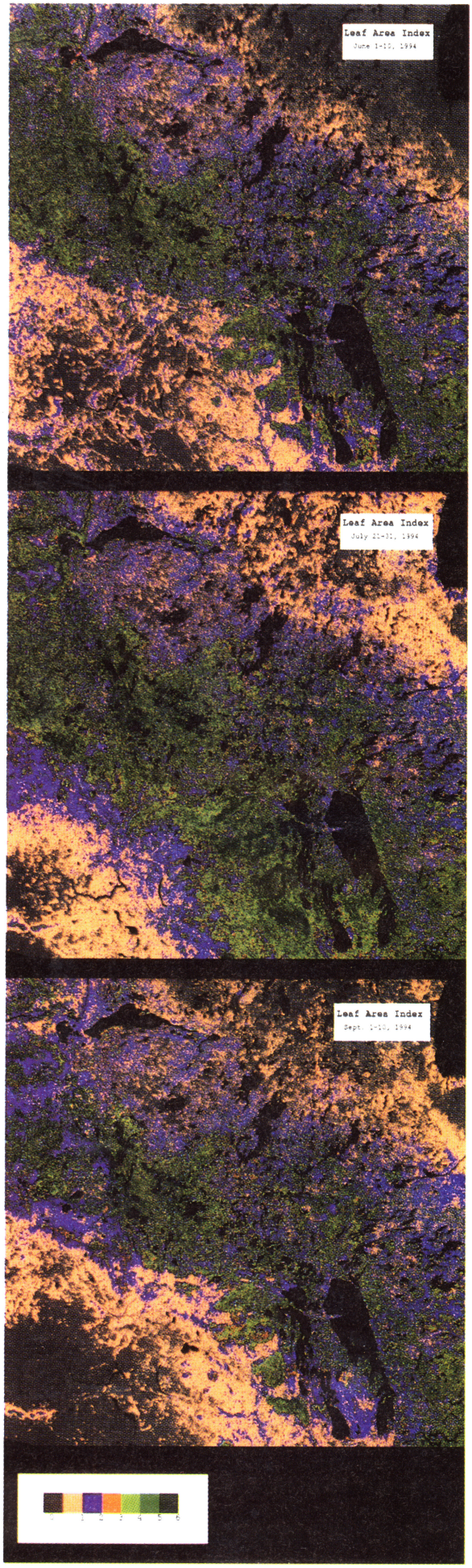

FPAR of the overstory was calculated from the downwelling and upwelling PAR measurements at two levels (above and below the overstory) in over 30 stands. The below-canopy measurements were made using the TRAC. Since the downwelling PAR through the overstory and upwelling PAR reflected from the forest floor are highly variable, average values were obtained from many closely spaced measurements over long transects (50–340 m). Simultaneous measurements of the downwelling and upwelling PAR above the forest were made on BOREAS meteorological towers [*Sellers et al.*, 1995]. The data were collected at the beginning, middle, and end of growing season to consider the effect of seasonal vegetation dynamics and the change in solar zenith angle [*Chen*, 1996b].

3.5. Absorbed Photosynthetically Active Radiation (APAR)

FPAR is a measure of the capacity of a canopy in intercepting visible solar energy (wavelengths 400–700 nm) during the photosynthetic process. The actual photosynthesis rate is, however, determined by the amount of PAR absorbed by the green canopy, APAR. By definition, APAR is related to FPAR by

$$\mathrm{APAR} = \mathrm{PAR} * \mathrm{FPAR}, \tag{4}$$

where PAR denotes downwelling PAR incident at the top of the canopy (TOC). While a few methods exist to retrieve PAR from satellite measurements [*Frouin and Pinker*, 1995], these are generally complex and susceptible to errors, primarily because of the inadequate knowledge of cloud properties [*Li and Moreau*, 1996]. Since cloud droplets do not have absorption bands across the PAR spectral region, one should be able to determine more readily and accurately the total amount of PAR absorbed in the surface layer below the TOC, $\mathrm{APAR}_{\mathrm{SFC}}$ [*Li and Moreau*, 1996]. PAR can then be computed from $\mathrm{APAR}_{\mathrm{SFC}}$ with the knowledge of PAR surface albedo A_{PAR}:

$$\mathrm{PAR} = \frac{\mathrm{APAR}_{\mathrm{SFC}}}{1 - A_{\mathrm{PAR}}}. \tag{5}$$

The FPAR products discussed above (Plate 6) can thus be employed to compute APAR using the expression

$$\mathrm{APAR} = \frac{\mathrm{APAR}_{\mathrm{SFC}}}{1 - A_{\mathrm{PAR}}} * \mathrm{FPAR}. \tag{6}$$

On the basis of extensive atmospheric radiative transfer modeling, a parameterization was developed to estimate $\mathrm{APAR}_{\mathrm{SFC}}$ from satellite visible measurements with only three parameters: the Sun angle, aerosol, and ozone amount. The parameterization, albeit extremely simple, is applicable to any sky condition and is able to reproduce the results of a far more complex radiative transfer model to within 5 W m^{-2} [*Li and Moreau*, 1996]. Its performance was evaluated using satellite and surface measurements from both the First ISLSCP Field Experiment (FIFE) [*Li and Moreau*, 1996] and the BOREAS [*Li et al.*, 1996]. The comparisons show small bias errors and moderate random errors. Random errors were attributed mainly to the mismatch between satellite and surface measurements in time and space.

Over a large area, A_{PAR} can be derived from clear-sky sat-

Plate 5. (opposite) Leaf area index for the BOREAS region for the three intensive field campaigns: (top) IFC-1, June 1–10; (middle) IFC-2, July 21–31; and (bottom) IFC-3, September 1–10.

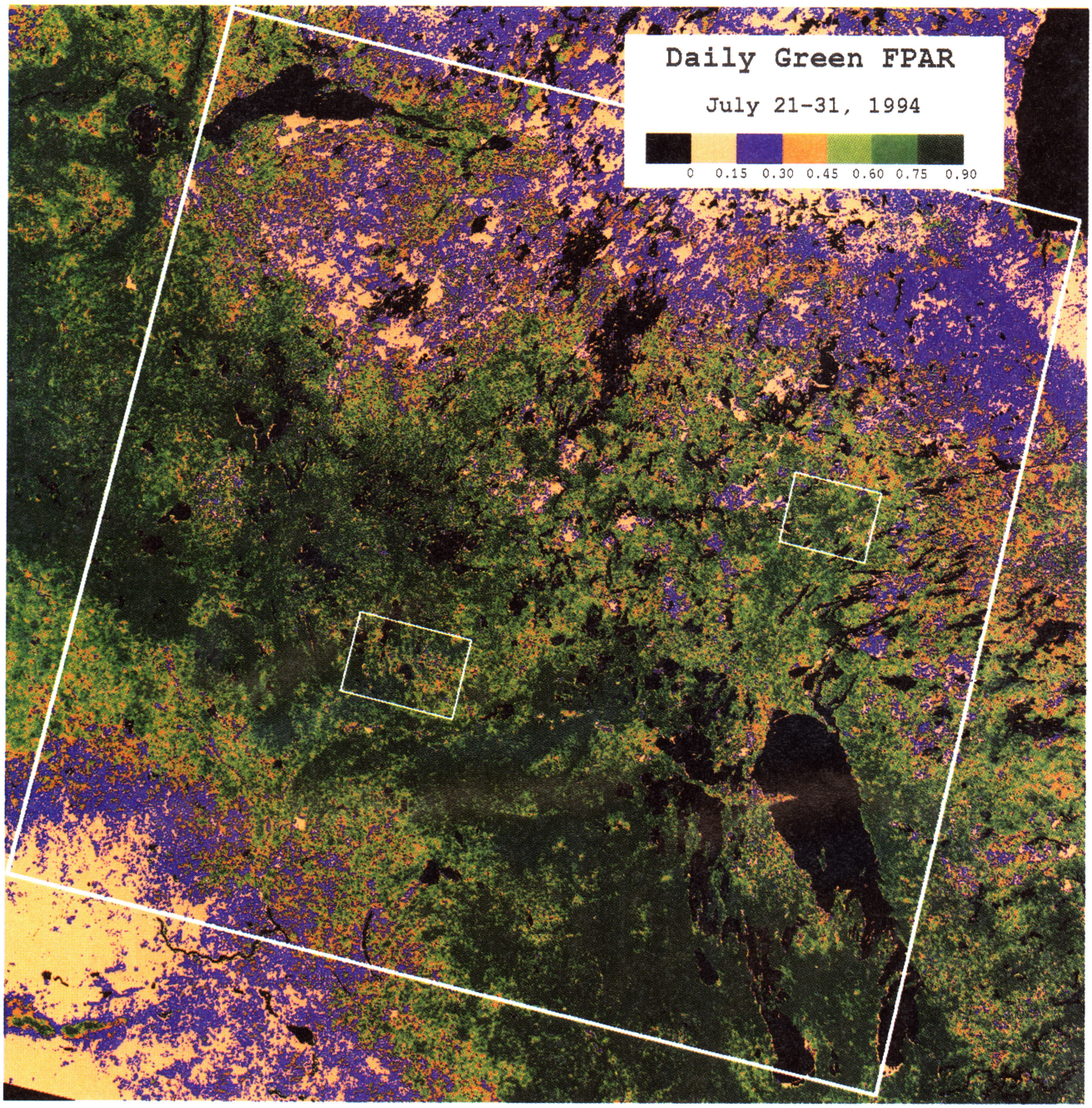

Plate 6. Fraction of photosynthetically active radiation for the BOREAS region during IFC-2 (July 21–31, 1994). The three squares outline the BOREAS region and the northern and southern study areas, respectively.

ellite data in the visible channel such as the AVHRR channel 1. When satellite data are used, the estimation of A_{PAR} involves four major steps: cloud screening, atmospheric correction, bidirectional correction, and spectral correction. The first three steps have been addressed above. The last step accounts for the spectral difference between the band pass of the visible sensor in question and the PAR spectral band. Conversion models for various sensors under a range of atmospheric and surface conditions were obtained from radiative transfer modeling [*Li and Moreau*, 1996]. For most terrestrial surfaces the difference between A_{PAR} and the albedo over the spectral region of AVHRR/1 is very small. Plate 7 (right panel) provides an example of PAR albedo derived from the composite during the period July 21–31, 1994, over the BOREAS study region. The values are generally small, less than 0.06 for most of the region. Nevertheless, they show some variability, primarily in response to land cover types. The lowest PAR albedo values occur in the coniferous forests (around 0.03 ~ 0.04, in agreement with ground observations) and the highest in the cropland (about 0.1). A few scattered pixels larger than 0.15 are likely due to remaining cloud contamination.

Daily and monthly mean APAR products over the BOREAS study region in the summer of 1994 have been generated from AVHRR measurements. As an example, the distributions of PAR and APAR on July 25, 1994, are presented in Plate 7. The variation of PAR (Plate 7, left) is governed by cloud cover. Regions of PAR below 110 W m^{-2} correspond to widespread cloud decks. In addition to cloud, PAR is also seriously af-

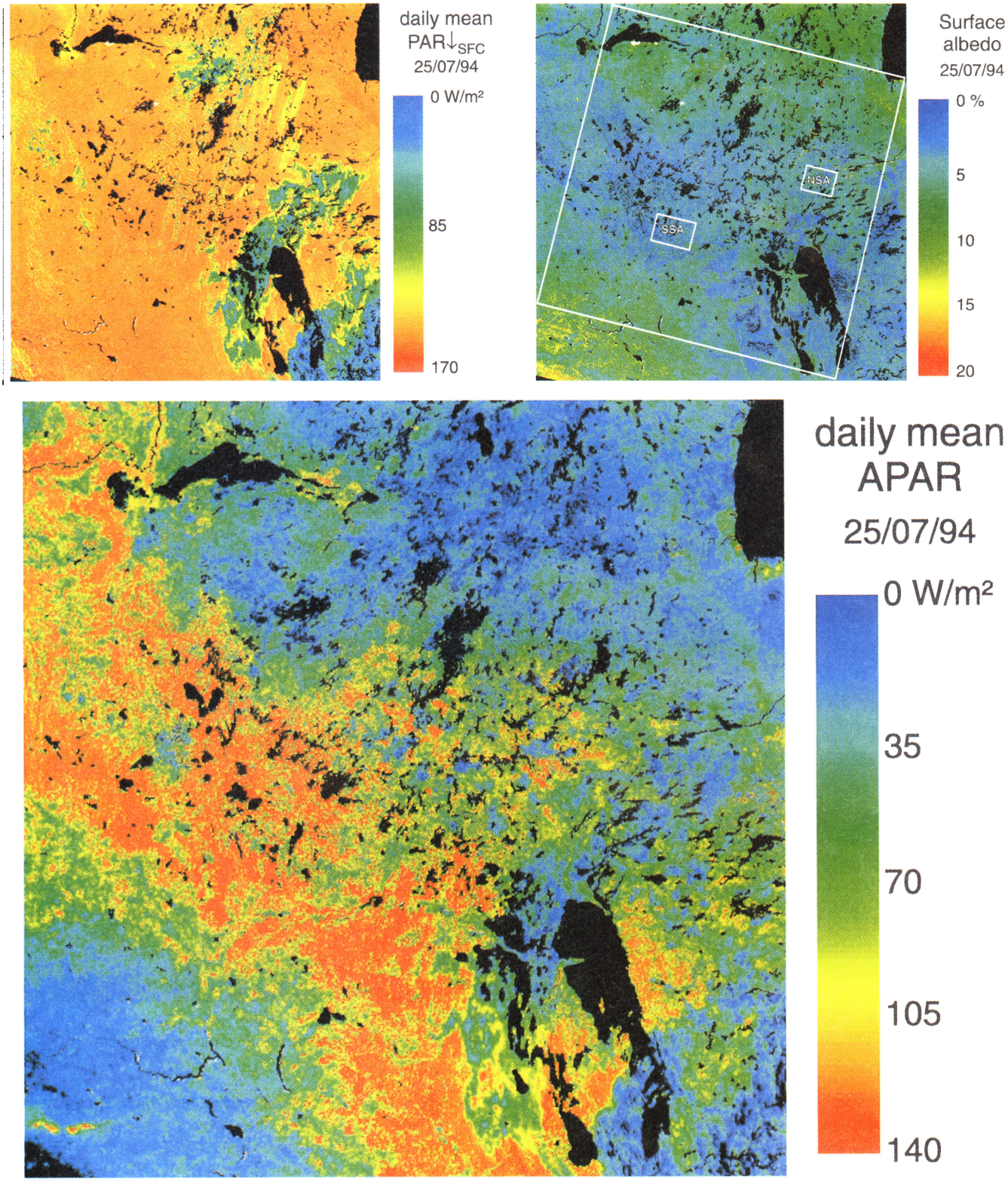

Plate 7. Absorbed photosynthetically active radiation (APAR) over the BOREAS region on July 25, 1994 (IFC-2). (Left) PAR incident at top of canopy, (right), PAR albedo, and (bottom) APAR absorbed by green phytomass.

fected by the smoke produced from forest fires. Fire was very active around the BOREAS study region in June and July 1994 [*Li et al.*, this issue (a)]. Hundreds of fires were detected from both ground-based and space-based observations during the growing season. Most of them were located in the north of the BOREAS study region [*Li et al.*, this issue (a)]. On July 25, 1994, numerous smoke plumes were visible in the top right-hand and left-hand portions of Plate 7 (left panel) with PAR ranging from 115 to 130 W m^{-2}. Over clear regions, PAR was generally greater than 145 W m^{-2}.

The distribution of APAR (Plate 7, bottom) exhibits a very different pattern from that of PAR. Apart from the influence of cloud, APAR is affected mostly by the amount of green vegetation. The top right-hand corner of Plate 7 (bottom panel) is the northern transitional forest and the bottom left corner is primarily cropland. Both areas have less green vegetation cover and hence smaller FPAR than the central area occupied by the boreal forest. APAR, being the product of PAR and FPAR, is affected by both the cloud pattern and the amount of green vegetation.

4. Summary and Conclusions

The derivation of biophysical parameters from satellite optical data is complicated due to the several factors that interfere with the relationship between the recorded electromagnetic signal and the environmental attribute of interest. In general, they belong to three domains: sensor, intervening atmosphere, and target. In developing the parameterization of satellite data for the estimation of surface properties (such as LAI), much attention is typically given to the relationship between incident and reflected radiation at the ground level and the property of interest. While this is essential because of the complex nature of the within-canopy radiation transfer, the existence of superior algorithms is not sufficient for producing quality data set over large areas. Equally important is the preparation of satellite data to the form with which such algorithms can be effectively coupled. Aside from the atmospheric and viewing angle effects which are common to other geographic regions, the unique challenges in northern areas are extreme solar zenith angles and intermittent snow cover near the ends of the growing season, and the smoke from fires in the boreal forest during the growing season.

The above results and those of others [e.g., *Goward et al.*, 1994] suggest that satellite data can provide useful estimates of parameters describing the surface radiation environment within which ecosystem processes take place. The bias and random errors present in such products can be established by a combination of modeling, field measurements, and the use of higher-resolution remote sensing data [*Cihlar et al.*, 1997]. Since the satellite products can be generated over large areas and repeatedly, the scaling of processes through models nourished by these data products is feasible. The future challenge will be in transferring the procedures among satellite sensors, in maintaining a rigorous quality control program so that the derived products can be generated over many years, and in acquiring sufficient ongoing field measurements to ensure that the models continue to represent the actual processes. The combined efforts of modeling and data set generation will thus produce a much improved understanding of the ecosystem-atmosphere interactions at daily to decadal timescales.

Acknowledgments. We are pleased to acknowledge the contribution of the staff at the Manitoba Remote Sensing Centre who produced the initial GEOCOMP data set: Pat Hurlburt, Hartley Pokrant, and Roy Dixon. Fengting Huang and Hung Ly (Intermap Information Technologies Ltd.) carried out many of the postprocessing operations. Sylvain Leblanc and Louis Moreau (Intermap Information Technologies Ltd.) contributed to the development of the LAI and APAR algorithms, respectively.

References

Aase, J. K., J. P. Millard, and B. S. Brown, Spectral radiance estimates of leaf area and leaf phytomass of small grains and native vegetation, *IEEE Trans. Geosci. Remote Sens.*, *24*, 685–692, 1986.

Ahern, F. J., R. P. Gauthier, P. M. Teillet, J. Sirois, G. Fedosejevs, and D. Lorente, An investigation of continental aerosols with high resolution solar extinction measurements, *Appl. Op.*, *30*, 5276–5287, 1991.

Asrar, G., M. Fuchs, E. T. Kanemasu, and J. H. Hatfield, Estimating absorbed photosynthetic radiation and leaf area index from spectral reflectance in wheat, *Agron. J.*, *76*, 300–306, 1984.

Becker, F., and Z. L. Li, Towards a local split window method over land surface, *Int. J. Remote Sens.*, *3*, 369–393, 1990.

BOREAS Science Steering Committee, BOREAS (Boreal Ecosystem-Atmosphere Study): Global change and biosphere-atmosphere interactions in the boreal forest biome, in *Science Plan*, 31 pp. plus appendix, NASA, Greenbelt, Md., 1991.

Chen, J. M., Optically-based methods for measuring seasonal variation in leaf area index in boreal conifer stands, *Agric. For. Meteorol.*, *80*, 135–163, 1996a.

Chen, J. M., Canopy architecture and remote sensing of the fraction of photosynthetically active radiation absorbed by boreal conifer forests, *IEEE Trans. Geosci. Remote Sens.*, *34*, 1353–1368, 1996b.

Chen, J. M., Evaluation of vegetation indices and a modified simple ratio for boreal applications, *Can. J. Remote Sens.*, *22*, 229–242, 1996c.

Chen, J. M., and T. A. Black, Defining leaf area index for non-flat leaves, *Plant Cell Environ.*, *15*, 421–429, 1992.

Chen, J. M., and J. Cihlar, Plant canopy gap size analysis theory for improving optical measurements of leaf area index, *Appl. Op.*, *34*, 6211–6222, 1995a.

Chen, J. M., and J. Cihlar, Quantifying the effect of canopy architecture on optical measurements of leaf area index using two gap size analysis methods, *IEEE Trans. Geosci. Remote Sens.*, *33*, 777–787, 1995b.

Chen, J. M., and J. Cihlar, Retrieving leaf area index of boreal conifer forests using Landsat TM images, *Remote Sens. Environ.*, *55*, 153–162, 1996.

Chen, J. M., P. D. Blanken, T. A. Black, M. Guilbeault, and S. Chen, Radiation regime and canopy architecture in a boreal aspen forest, *Agric. For. Meteorol.*, *86*, 107–125, 1997.

Chen, J. M., P. M. Rich, T. S. Gower, J. M. Norman, and S. Plummer, Leaf area index of boreal forests: Theory, techniques, and measurements, *J. Geophys. Res.*, this issue.

Cihlar, J., Identification of contaminated pixels in AVHRR composite images for studies of land biosphere, *Remote Sens. Environ.*, *56*, 149–163, 1996.

Cihlar, J., and P. M. Teillet, Forward piecewise linear model for quasi-real time processing of AVHRR data, *Can. J. Remote Sens.*, *21*, 22–27, 1995.

Cihlar, J., T. Sommerfeldt, and B. Patterson, Soil water content estimation in fallow fields from airborne thermal scanner measurements, *Can. J. Remote Sens.*, *5*, 18–32, 1979.

Cihlar, J., D. Manak, and M. D'Iorio, Evaluation of compositing algorithms for AVHRR over land, *IEEE Trans. Geosci. Remote Sens.*, *32*, 427–437, 1994.

Cihlar, J., J. Chen, and Z. Li, On the validation of satellite-derived products for land applications, *Can. J. Remote Sens.*, in press, 1997.

Cihlar, J., H. Ly, and Q. Xiao, Land cover classification with AVHRR multichannel composites in northern environments, *Remote Sens. Environ.*, *58*, 36–51, 1996.

Cihlar, J., H. Ly, Z. Li, J. Chen, H. Pokrant, and F. Huang, Multitemporal, multichannel AVHRR data sets for land biosphere studies–Artifacts and corrections, *Remote Sens. Environ.*, *60*, 35–57, 1997.

Coll, C., V. Caselles, J. A. Sobrino, and E. Valor, On the atmospheric dependence of the split-window equation for land surface temperature, *Int. J. Remote Sens.*, *15*, 105–122, 1994.

Czajkowski, K. P., T. M. Mulhern, S. N. Goward, and J. Cihlar, Validation of the Geocoding and Compositing System (GEOCOMP) using contextual analysis of AVHRR images, *Int. J. Remote Sens.*, *18*, 3055–3068, 1997.

Eidenshink, J. C., and J. L. Faundeen, The 1 km AVHRR global land data set: First stages in implementation, *Int. J. Remote Sens.*, *15*, 3443–3462, 1994.

Frouin, R., and R. T. Pinker, Estimating photosynthetically active radiation (PAR) at the earth's surface from satellite observations, *Remote Sens. Environ.*, *51*, 98–107, 1995.

Gardner, B. R., and B. L. Blad, Evaluation of spectral reflectance models to estimate corn leaf area while minimizing the influence of soil background effects, *Remote Sens. Environ.*, *20*, 183–193, 1986.

Gatlin, J. A., R. J. Sullivan, and C. J. Tucker, Considerations of and improvements to large-scale vegetation monitoring, *IEEE Trans. Geosci. Remote Sens., GE-22*, 496–502, 1984.

Goward, S. N., R. H. Waring, D. G. Dye, and J. Yang, Ecological remote sensing at OTTER: Satellite macroscale observations, *Ecol. App., 4*, 322–343, 1994.

Holben, B., Characteristics of maximum-value composite images from temporal AVHRR data, *Int. J. Remote Sens., 7*, 1417–1434, 1986.

Holben, B. N., C. J. Tucker, and C-J. Fan, Spectral assessment of soybean leaf area and leaf biomass, *Photogram. Eng. Remote Sens., 46*, 651–656, 1980.

James, M. E., and S. N. V. Kalluri, The Pathfinder AVHRR land data set: An improved coarse resolution data set for terrestrial monitoring, *Int. J. Remote Sens., 15*, 3347–3363, 1994.

Kidwell, K. B., *NOAA Polar Orbiter Data User's Guide*, Natl. Oceanic and Atmos. Admin., Natl. Environ. Satellite Data and Inf. Serv., Washington, D. C., 1991.

Li, Y., T. H. Demetriades-Shah, E. T. Kanemasu, J. K. Shultis, and M. B. Kirkham, Use of second derivatives of canopy reflectance for monitoring prairie vegetation over different soil backgrounds, *Remote Sens. Environ., 44*, 81–87, 1993.

Li, Z., and L. Moreau, A new approach for estimating photosynthetically active radiation absorbed by canopy from space, I, Total surface absorption, *Remote Sens. Environ., 55*, 175–191, 1996.

Li, Z., J. Cihlar, X. Zhang, L. Moreau, and H. Ly, Detection and correction of the bidirectional effects in AVHRR measurements over northern regions, *IEEE Trans. Geosci. Remote Sens., 34*, 1308–1322, 1996.

Li, Z., J. Cihlar, L. Moreau, F. Huang, and B. Lee, Monitoring fire activities in the boreal ecosystem, *J. Geophys. Res.*, this issue (a).

Li, Z., L. Moreau, and J. Cihlar, Estimation of the photosynthetically active radiation absorbed at the surface, *J. Geophys. Res.*, this issue (b).

Moreau, L., and Z. Li, A new approach for estimating photosynthetically active radiation absorbed by canopy from space, II, Proportion of canopy absorption, *Remote Sens. Environ., 55*, 192–204, 1996.

Newcomer, J., and J. Cihlar, BOREAS level-2 advanced very high resolution radiometer (AVHRR) composite data, The BOREAS Information System, NASA, 12 pp., 1995.

Planet, W. G., Data extraction and calibration of TIROS-N/NOAA radiometers, NOAA Tech. *Memo., NESS 107*, U.S. Dep. of Comm., Washington, D. C., 1988.

Pokrant, H., Land cover map of Canada derived from AVHRR images, Manitoba Remote Sens. Cent., Winnipeg, Manitoba, Canada, 1991.

Rahman, H., and G. Dedieu, SMAC: A simplified method for the atmospheric correction of satellite measurements in the solar spectrum, *Int. J. Remote Sens., 15*, 123–143, 1994.

Robertson, B., A. Erickson, J. Friedel, B. Guindon, T. Fisher, R. Brown, P. Teillet, M. D'Iorio, J. Cihlar, and A. Sancz, GEOCOMP, a NOAA AVHRR geocoding and compositing system, Proceedings of the ISPRS Conference, Commission 2, Washington, D.C.: 223–228, 1992.

Roujean, J.-L., M. Leroy, and P.-Y. Deschamps, A bidirectional reflectance model of the earth's surface for the correction of remote sensing data, *J. Geophys. Res., 97*, 20,455–20,468, 1992.

Saint, G., VEGETATION onboard SPOT 4: Products specification, VEGETATION Int. Users Comm., Ispra, Italy, 1994.

Salisbury, J. W., and M. D. D'Aria, Emissivity of terrestrial materials in the 8–14 mm atmospheric window, *Remote Sens. Environ., 42*, 83–106, 1992.

Salomonson, V. V. The moderate resolution imaging spectrometer (MODIS), *IEEE Geosci. Remote Sens. Newslett., 12*, 11–15, 1988.

Sellers, P. J., S. O. Los, C. J. Tucker, C. O. Justice, D. A. Dazlich, J. A. Collatz, and D. A. Randall, A global 1° by 1° NDVI data set for climate studies, 2, The generation of global fields of terrestrial biophysical parameters from the NDVI, *Int. J. Remote Sens., 15*, 3519–3545, 1994.

Sellers, P., et al., The Boreal Ecosystem-Atmosphere Study (BOREAS): An overview and early results from the 1994 field year, *Bull. Am. Meteorol. Soc., 76*, 1549–1577, 1995.

Tanre, D., et al., Description of a computer code to simulate the satellite signal in the solar spectrum, *Int. J. Remote Sens., 11*, 659–668, 1990.

Teillet, P. M., An algorithm for the radiometric and atmospheric correction of AVHRR data in the solar reflective channels, *Remote Sens. Environ., 41*, 185–195, 1992.

Teillet, P. M., and B. N. Holben, Towards operational radiometric calibration of NOAA AVHRR imagery in the visible and near-infrared channels, *Can. J. Remote Sens., 20*, 1–10, 1994.

Van de Griend, A. A., and M. Owe, On the relationship between thermal emissivity and the normalized difference vegetation index for natural surfaces, *Int. J. Remote Sens., 14*, 1119–1131, 1993.

Wiegand, C. L., S. J. Maas, J. K. Aase, J. L. Hatfield, P. J. Pinter, Jr., R. D. Jackson, E. T. Kanemasu, and R. L. Lapitan, Multisite analyses of spectral-biophysical data for wheat, *Remote Sens. Environ., 42*, 1–21, 1992.

Wooster, M. J., T. S. Richards, and K. Kidwell, NOAA-11 AVHRR/2—Thermal channel calibration update, *Int. J. Remote Sens., 16*, 359–363, 1995.

Wu, A., Z. Li, and J. Cihlar, Effects of land cover type and greenness on advanced very high resolution radiometer bidirectional reflectances: Analysis and removal, *J. Geophys. Res., 100*, 9179–9192, 1995.

J. Cihlar and Z. Li, CCRS Natural Resources Canada, Fourth Floor, 588 Booth Street, Ottawa, Ontario, K1A 0Y7, Canada. (e-mail: josef.cihlar@ccrs.nrcan.gc.ca)

(Received June 4, 1996; revised March 11, 1997;
accepted March 26, 1997.)